AIAA JOURNAL
Vol. 47, No. 9, September 2009

Computational Study of Helicopter Rotor–Fuselage Aerodynamic Interactions

R. Steijl* and G. N. Barakos†
University of Liverpool, Liverpool, England L63 3GH, United Kingdom

DOI: 10.2514/1.41287

Aerodynamic interactions between the main rotor, fuselage, and tail rotor must be considered during the design phase of a helicopter, and their effect on performance must be quantified. However, interactional helicopter aerodynamics has so far been considered by very few researchers. In this work, the Helicopter Multi-Block flow solver is used to investigate the flow around two generic rotor–fuselage cases before moving on to a more realistic full-helicopter geometry under investigation in the European Commission Framework 6 Generation of Advanced Helicopter Experimental Aerodynamic Database project. A comparison of the computational fluid dynamics results obtained with experimental data shows that the method is capable of resolving the main interactional flow features for the generic cases. A similar comparison with experimental data for the Generation of Advanced Helicopter Experimental Aerodynamic Database test case has not yet been conducted, but the obtained results show that even for a test case of high complexity, state-of-the-art rotorcraft computational fluid dynamics methods are capable of providing realistic predictions. However, comparisons with isolated rotor cases clearly show the increased loading as the blade passes over the nose of the helicopter as the result of a fuselage-induced upwash. Similarly, the fuselage induces a reduction of the blade loading for inboard stations when the blades passes through the rear part of the rotor disk. The present results highlight and quantify the radial and azimuthal extent of the rotor–fuselage interactional effect on the rotor loading.

Nomenclature

AR	=	rotor aspect ratio, R/c
a_∞	=	freestream speed of sound, m/s
C_N	=	section normal force coefficient (blade section axes)
C_T	=	rotor thrust coefficient, $T/(\rho_\infty(\Omega R)^2\pi R^2)$
C_p	=	pressure coefficient, $(p-p_\infty)/q_\infty$
c	=	(mean) rotor chord, m
M_r	=	relative Mach number, $M_{\text{tip}}[r/R\cos(\lambda) + \mu\sin(\psi-\lambda)]$
M_{tip}	=	rotational Mach number, $\Omega R/a_\infty$
M_∞	=	freestream Mach number
M^2C_p	=	$(p-p_\infty)/(\frac{1}{2}\gamma p_\infty)$
p_∞	=	freestream pressure, Pa
q_r	=	relative dynamic pressure, $\frac{1}{2}\rho_\infty(\Omega r + U_\infty\sin(\psi-\lambda))^2$, Pa
q_∞	=	freestream dynamic pressure, $\frac{1}{2}\rho_\infty U_\infty^2$, Pa
R	=	rotor radius, m
r	=	radial coordinate along rotor blade, m
U_∞	=	freestream velocity, m/s
λ	=	(local) blade sweep angle, deg
μ	=	rotor advance ratio
ρ_∞	=	freestream density, kg/m^3
σ	=	rotor solidity, $N_{\text{blades}}/\pi\text{AR}$
ψ	=	blade azimuth (0 deg at rear of rotor disk), deg
Ω	=	rotor rotation rate, rad/s

I. Introduction

PREDICTION of aerodynamic interactions between the main rotor, tail rotor, and fuselage is crucial for performance analysis of helicopter configurations. Regardless of its importance, interactional helicopter aerodynamics has so far been considered by few researchers, due to a number of reasons. First, the aeromechanics of an isolated rotor is still a very challenging area, because it constitutes a complex multidisciplinary problem involving vortical wake flows, transonic flow regions, rotor blade dynamics, and elastic blade deformation. The second reason for the limited number of studies in interactional aerodynamics is the geometric complexity and even more complex flow physics involved in rotor–fuselage or full-helicopter configurations. Only recent studies [1–4] suggest that computational fluid dynamics (CFD) methods could perhaps tackle such complex flows. For the preceding reasons, most of the published works concern wind-tunnel experiments with generic helicopter rotors mounted over idealized fuselage shapes: for example, the rotor–cylinder test case of Georgia Institute of Technology (Georgia Tech) [5–8] and the rotor–body interaction (ROBIN) test case of NASA [9–13]. In the first example, the airframe is represented by a circular cylinder with hemispherical nose, whereas the ROBIN case is closer to a helicopter fuselage shape, but tail planes, engine inlets, exhausts, etc., are ignored.

The importance of helicopter interactional aerodynamics combined with the progress in CFD algorithms and the availability of powerful affordable computers encouraged a few recent CFD studies [2,4,14–19]. These investigations have not yet reached the maturity of numerical investigations of hovering rotors or isolated rotors in forward flight and there are a number of contributing factors for this. At first, the geometric complexity of a rotor–fuselage or a full-helicopter configuration is high, and the resulting task to generate good-quality CFD meshes is challenging. In addition, the complexity of CFD methods capable of solving the flow around a helicopter is increased, due to the need to handle relative motions of rotor blades and fuselages. Finally, a third major factor is the lack of adequate wind-tunnel flight-test data for validation purposes.

Therefore, an urgent need exists for a database of high-quality experimental data that can act as validation for the state-of-the-art CFD methods. To address this need, the European Commission funded the Framework 6 Program GOAHEAD (Generation of Advanced Helicopter Experimental Aerodynamic Database), with the aim to create such an experimental database and to validate state-of-the-art CFD methods. The CFD Laboratory at Liverpool University is involved in the CFD work package of this project, using the

Received 28 September 2008; revision received 11 February 2009; accepted for publication 31 May 2009.

*Research Associate, CFD Laboratory, Department of Engineering; R.Steijl@Liverpool.ac.uk.

†Reader, CFD Laboratory, Department of Engineering; G.Barakos@Liverpool.ac.uk.

Helicopter Multi-Block (HMB) flow solver [1,2]. The HMB solver uses a sliding-grid technique to handle the relative motion of the rotor (s) and the helicopter fuselage.

The present paper is structured as follows. First, a review of published experimental and numerical investigations into helicopter interactional aerodynamics is presented in Sec. II. Then the CFD method used in the present study is described in Sec. III. Section V presents the results for the Georgia Tech teetering rotor test case, and the ROBIN rotor-body test case is described in Sec. V. Results for the NH90-like geometry under investigation in the GOAHEAD project are presented in Sec. VI. Finally, conclusions are drawn in Sec. VII, along with future research plans.

II. Review of Previous Work

In the present work, the well-known Georgia Tech rotor–cylinder test case [5–7] and the ROBIN rotor–fuselage test case [9–13] are used for validation of the present CFD method as well as for the analysis of interactional aerodynamics of simple fuselage shapes.

In the Georgia Tech experiments, a simple two-bladed teetering rotor is considered, mounted on a cylindrical airframe with a hemispherical nose. The surface pressure measurements for this series of experiments were presented by Brand et al. [5]. Velocity field measurements for this configuration were also presented in the late 1980s by Liou et al. [6,7].

In their work, Kim and Komerath [8] presented a summary of experimental works for the interaction of the wake of simple two-bladed rotors with a cylindrical airframe. In addition, they presented comparisons of the experimental results with results from theoretical modeling of the interaction. The paper described the differences between the wake–fuselage interaction at the front of the rotor disk with that at the aft part. Building on potential flow models, the authors describe the wake–fuselage interaction in two phases: that is, a precollision phase in which the wake vortex trajectory is modified by the presence of the fuselage and a collision phase dominated by complex vortex–boundary-layer interactions. The precollision phase can be modeled with potential flow theory, whereas the collision phase obviously requires viscous flow models. The forward shaft tilt in the rotor–cylinder test cases was also considered, and the closer proximity of the rotor and the cylinder at the front of the disk, as compared with the separation of the rotor disk from the cylinder at the back, led to a qualitatively different behavior of the vortex path. In the theoretical model discussed by Kim and Komerath [8], the vortex wake descent is significantly decelerated relative to the isolated rotor wake development at the front of the rotor disk, whereas the deceleration is absent at the back. In the potential flow model, the interaction with the cylinder is different due to the opposite sense of vortex rotation at the front and back of the rotor disk; that is, at the front of the disk, the vortex can be expected to proceed directly to collide with the surface, whereas at the back, the vortex can be expected to have a less direct interaction, as it travels along the surface. Naturally, vortex–boundary-layer interactions will play an important role, particularly when the interaction leads to flow separation on the cylinder–fuselage. This set of results and observations highlights the difficulty in developing theoretical models for wake–fuselage interaction. In more recent studies, models including viscous effects have been discussed by Affes et al. [20,21].

The Georgia Tech rotor–cylinder test case and the ROBIN rotor–fuselage case have become standard test cases for CFD validation and as such have been simulated by various researchers using a range of different CFD techniques. An early numerical investigation of the rotor–cylinder problem based on potential flow methods was presented by Komerath et al. [22]. More recent work is typically based on the Euler equations or the Navier–Stokes equations and requires either the use of overset grids or a method based on a sliding-plane interface between the steady fuselage mesh and the rotor-fixed mesh. Alternatively, methods are used in which the rotor is not simulated, but its effect on the flow modeled through momentum source terms (i.e., actuator disk or actuator blade models). Hariharan and Sankar [23] represent an example of a study using an overset-grid Euler method for the Georgia Tech test case. Park et al. [15] and Park and Kwon [16] presented results for this test case from inviscid flow simulations with an unstructured-mesh sliding-plane method. The time-averaged pressure on the cylinder is characterized by two distinct peaks at the top of the model, where the rotor blades pass the cylinder. Interestingly, the predictions based on the Euler equations by both Hariharan and Sankar [23] and Park and Kwon [16] underpredict the peak of the averaged pressure present at the back of the rotor disk relative to the experimental data. The unstructured-mesh method of Park and Kwon was also used to simulate the ROBIN test case [16,17]. The comparison of the obtained results with experimental data demonstrated the capability to resolve the unsteady fuselage surface pressures due to the blade passage (i.e., the magnitude of the pressure fluctuations as well as the phasing agreed well), whereas in stations near the nose of the model, the mean value showed a modest discrepancy with the experimental data. Results obtained using the structured-mesh sliding-plane method used in the present study showed a very similar pattern [2].

In addition to the generic rotor–fuselage test cases, CFD methods have been successfully applied to more realistic configurations by a small number of research groups. The ongoing work at DLR, German Aerospace Center (DLR) and ONERA in developing CFD methods for the analysis of the flow around a full rotorcraft configuration was discussed by Sides et al. [14]. Both research centers have focused on developing chimera-based CFD methods for block-structured grids, which have been applied to realistic rotor–fuselage as well as full-helicopter configurations. Sides et al. presented initial results for the Eurocopter Dauphin 365N rotor–fuselage model, including an analysis of the influence of the fuselage on the blade loads at the rear of the rotor disk. A reduction in the blade loading was observed for the full helicopter on the inboard part of the rotor blade, relative to the equivalent isolated rotor result. Renaud et al. [18,19] presented a comparison of the computed unsteady fuselage pressures with experimental data for the Dauphin 365N rotor–fuselage model. Also, the predicted flowfield was compared with the experimental particle image velocimetry measurements, showing a favorable agreement of the predicted blade vortex positions with the experiments. In addition, results for the full NH90 geometry were presented. The flow around a BO105 wind-tunnel model, including main and tail rotors, was simulated at DLR [24,25]. The published work discussed the unsteady surface pressures in selected fuselage stations, showing a good agreement in the fluctuations, whereas the mean values show some discrepancies with the experimental data.

Potsdam et al. [26] presented a CFD analysis of the UH-60A main rotor using overset grids. The study included a coarse-grid solution for the rotor in the presence of a low-fidelity fuselage model. The presented results show an induced upwash on the inboard part of the rotor blade (i.e., within the first 40% blade radius) at the front of the rotor disk, thereby increasing the blade normal force.

The structured-mesh sliding-plane method used in the present study has been used previously for Navier–Stokes simulations of a realistic rotor–fuselage geometry under investigation in the European Commission GOAHEAD project [2].

Computational modeling techniques for complete rotorcraft configurations were also studied by O'Brien [27], who presented an analysis of the capability of actuator disk and actuator blade methods as well as overset-grid techniques to model rotor–fuselage interactional aerodynamics. The different techniques were implemented in the FUN3D unstructured-mesh CFD method. For the ROBIN and Georgia Tech test cases, the rotor-induced unsteady pressures on the fuselage were well captured for both the overset-grid simulation and the unsteady actuator blade method. In the unsteady actuator blade method, the rotor blades are not explicitly modeled, but their effect is modeled by applying unsteady momentum sources in the Navier–Stokes equations as functions of time and azimuthal position. Various blade loadings were studied, showing that the best results were obtained using blade-element theory for the blade loads. For the ROBIN case, the results for this model were comparable with the results obtained from the full unsteady overset-grid simulation. The actuator disk and actuator blade techniques were shown to be capable of predicting unsteady fuselage loads to

varying levels, whereas these models cannot predict the fuselage-induced changes on the rotor loads. Also, for the overset-grid results for the ROBIN, this fuselage influence on the rotor loads was not presented.

III. Sliding-Plane CFD method

A. HMB Flow Solver

The Helicopter Multi-Block CFD code [1–4] was employed for this work. HMB solves the unsteady Reynolds-averaged Navier–Stokes equations on block-structured grids using a cell-centered finite volume method for spatial discretization. Implicit time integration is employed, and the resulting linear systems of equations is solved using a preconditioned generalized conjugate gradient method. For unsteady simulations, an implicit dual-time-stepping method is used, based on Jameson's pseudotime integration approach [28]. The method has been validated for a wide range of aerospace applications and has demonstrated good accuracy and efficiency for very demanding flows. Examples of work with HMB can be found in [1,2,4,29–31]. Several rotor trimming methods are available in HMB, along with a blade-actuation algorithm that allows for the near-blade grid quality to be maintained on deforming meshes [1].

The HMB solver has a library of turbulence closures that includes several one- and two-equation turbulence models and even non-Boussinesq versions of the k-ω model. Turbulence simulation is also possible using either the large-eddy or the detached-eddy approach. The solver was designed with parallel execution in mind, and the message-passing-interface library along with a load-balancing algorithm are used to this end. For multiblock grid generation, the ICEM-CFD Hexa commercial meshing tool is used, and CFD grids with 10–20 million points and thousands of blocks are commonly used with the HMB solver.

B. Sliding-Plane Method

The underlying idea behind the sliding-mesh approach can be explained using Fig. 1, which shows the definition of two layers of halo cells around the boundary surface of each block. In the sliding-plane algorithm, this concept is extended to deal with grids that are discontinuous across the interface and can also be in relative motion. Figure 1b presents a situation in which two adjacent blocks have nonmatching cell faces. If the halo cells of each block are populated with interpolated values of the flowfield variables, the solver will have no difficulty in updating the flow solution. The application of the sliding-plane algorithm to nonmatching grids as well as grids in relative motion will result in nonmatching cell faces, as sketched in Fig. 1b. There are three main steps involved in populating the halo cells: 1) identification of the neighboring cells for each halo-cell, 2) interpolation of the solution at the centroids of the halo cells, and 3) exchange of information between blocks associated with different processors. The last step is important for computations on distributed-memory machines only. Regardless of the identification and interpolation methods employed, the halo-cell values are computed using

$$\phi_{\text{halo}} = \sum_{i=1}^{i=n} w_i \phi_i \tag{1}$$

where ϕ represents any flowfield variable, w_i is the weight associated with the ith neighbor of the halo cell, and n is the number of neighbors.

The distance-based interpolation (shown in Fig. 1c) computes a weighted sum of flowfield data of neighboring cells within an interaction radius. The weights are inversely proportional to the distance of the cell center from the projected point on the sliding-plane interface and are scaled to sum up to 1. Figure 1d shows the cell-face overlap interpolation, in which case the weight for each neighbor is directly proportional to the fraction of the projected cell-face area that overlaps with the cell face of this neighbor cell. In the context of finite volume discretization methods for conservation laws based on numerical fluxes through cell faces, the cell-face overlap interpolation is the preferred method. However, an interpolation method based on the overlap weighting of Fig. 1d does not necessarily enforce conservation and due to differences in grid sizes on both sides of the sliding-plane interface may act as a spatial filter.

The present implementation of the sliding-mesh algorithm is based on the cell-face overlap interpolation method presented in Fig. 1d. Sliding-mesh interfaces can be of arbitrary shape and for this reason the contributing cell surfaces must all be projected on the curvilinear ξ, η, and ζ axes as used in the present finite volume solver. This step can be combined with a transformation from primitive to

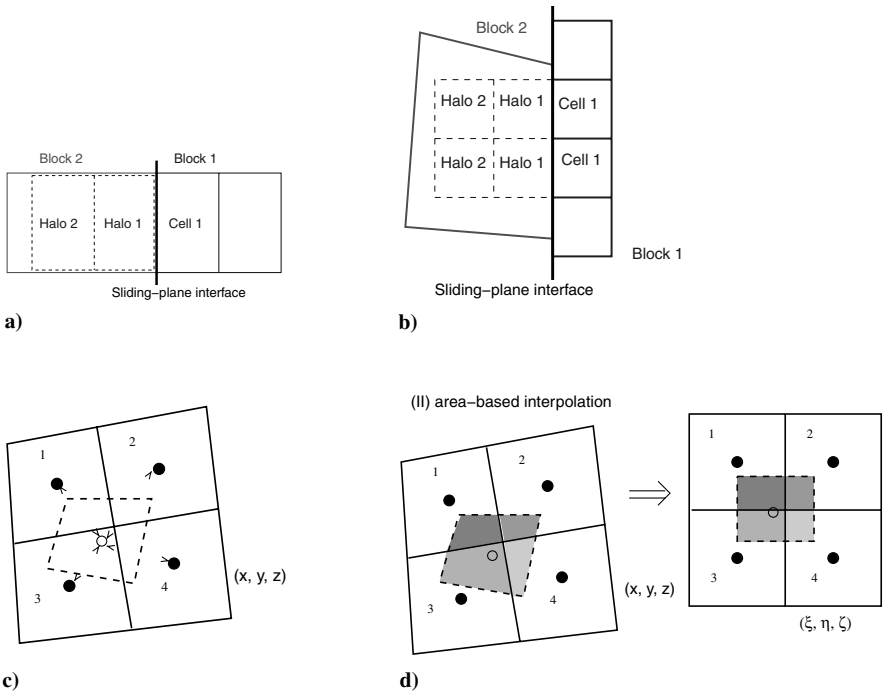

Fig. 1 Construction of halo-cell values along sliding-plane interfaces: a) matching cell faces, b) nonmatching cell faces, c) distance-based interpolation, and d) cell-area weighted interpolation.

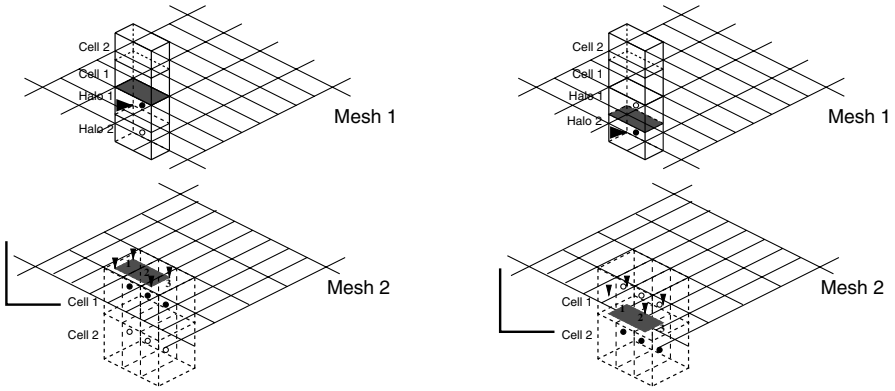

a) First layer of halo cells (mesh 1) **b) Second layer of halo cells (mesh 1)**

Fig. 2 Identification of neighbors along with cell-face overlap used to determine interpolation weights. Two layers of halo-cell values are set by projecting the cell face onto the sliding-plane interface. The cell faces of the adjacent mesh that overlap are neighbors, and for each neighbor, the fraction of the overlap corresponds to the interpolation weight.

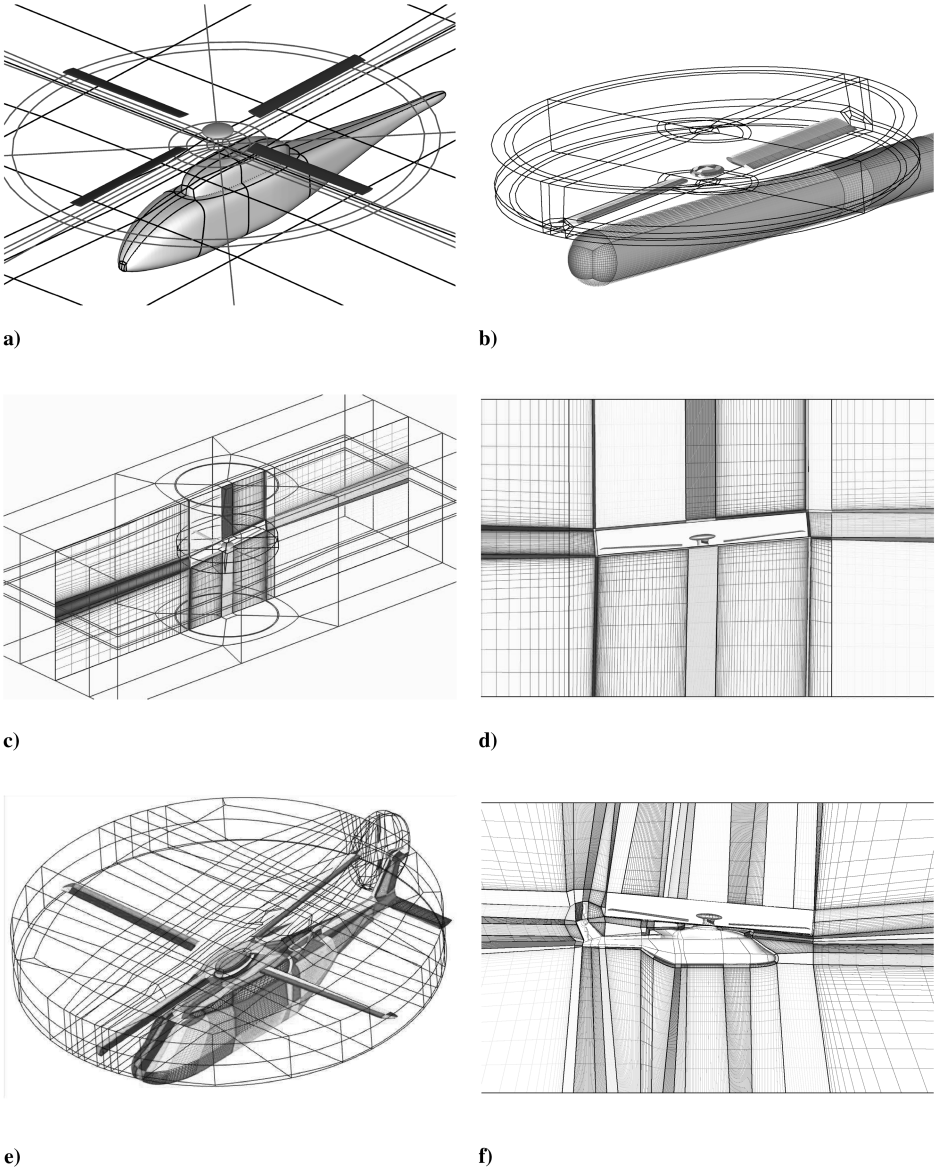

a) **b)**

c) **d)**

e) **f)**

Fig. 3 Sliding-plane approach for varying levels of geometric complexity: a) rotor–fuselage with one plane, b) rotor–body with three planes, c) rotor in tunnel with three planes, d) center plane for rotor–tunnel case, e) full helicopter with six planes, and f) center plane for full-helicopter case.

conservative variables so that flux-weighted summations can also be computed.

Figure 2 shows a sketch of the identification of neighbors as well as the interpolation weight computation used in the present method. Two layers of halo-cell values are set for each cell on the sliding plane (s). For nonplanar sliding interfaces, cells are projected on a plane before computing the area overlaps with their counterpart plane. The cell faces of the adjacent mesh that overlap are the neighbors. For each neighbor, the fraction of the overlap corresponds to the interpolation weight. The preceding procedure has been tested in validation test cases involving planar, cylindrical, and spherical sliding-plane interfaces. Also, the method has been implemented to handle an arbitrary number of sliding planes. This enables simulation of test cases at a high level of geometric complexity, as is discussed in the next section.

C. Application of the Sliding-Plane Method to Rotorcraft Aerodynamics

Figure 3 illustrates the application of the sliding-plane method to rotorcraft test cases of varying levels of geometric complexity. Figure 3a shows the ROBIN generic rotor–fuselage test case as an example of a rotor–fuselage case that can be modeled using a single planar sliding plane. This single plane can only be used when the model is not placed within a wind tunnel. Also, the sliding plane needs to be perpendicular to the rotor shaft; that is, the sliding plane will, in general, have an inclination relative to the fuselage centerline of around 3–5 deg. Assuming that far-field boundary conditions can be imposed on the domain outer surfaces, the actual shape of these outer surfaces can be chosen freely. In this case, the domain is defined with a cylindrical vertical bounding surface; that is, the fuselage grid is defined with a cylindrical far-field boundary that matches the far-field boundary of the rotor mesh. For more complex fuselage shapes than the ROBIN, the single planar sliding-plane interface may intersect parts of the geometry. In the present work, this problem is solved by defining a drum-shaped interface for which the rotor mesh does not extend to the far field of the nonrotating fuselage (background) mesh. In this approach, a drum-shaped cavity is defined within the fuselage mesh, in which the rotor mesh is placed. The interface is formed by a cylindrical sliding plane in the rotor radial direction, in addition to two planar sliding planes at the upper and lower bounding surfaces. In Fig. 3b, this approach is sketched for the Georgia Tech rotor–cylinder test case, for which a single sliding plane could also have been used. Figures 3c and 3d show an example of a rotor placed within a wind tunnel, for which case a drum-shaped interface between the rotor mesh and the stationary wind-tunnel mesh is used. Figures 3e and 3f show the application to a full-helicopter geometry, with both main and tail rotor. In the present work, two drum-shaped interfaces are defined, one for each rotor, with a total of six sliding-plane surfaces. The grid generation for this case is highly complex, because, in addition to the realistic fuselage geometry with fairings and exhausts, two drum-shaped cavities are required in which the rotor meshes are to be placed. The close proximity of the two rotors at the back of the main rotor disk poses an significant challenge in developing a multiblock topology for the fuselage mesh.

An important aspect in the present work is the flexibility that the sliding-plane method provides in reusing meshes. For example, the fuselage grid in Figs. 3e and 3f can be reused to study the flow around the isolated fuselage, by replacing the main and tail rotor meshes with drum-shaped grids without solid surfaces. Similarly, the contribution of the main rotor head vortex shedding to the unsteady tail plane loads can be investigated by replacing the main rotor mesh with a mesh for the main rotor head in isolation. Another possibility, used in the present work is the reuse of the main rotor grid to create a mesh for an isolated rotor simulation, by placing it in a grid for the wind tunnel without the fuselage, as shown in Figs. 3c and 3d. This enables a direct comparison of the rotor loads for the full helicopter with those predicted for the isolated case, while using exactly the same rotor grid.

The main advantage of the current method over chimera is the very low overhead in terms of CPU time. On the other hand, the sliding-mesh technique cannot account for intermeshing rotors and requires a careful placement of the interfaces. An additional requirement is to maintain similar grid densities on each of the sliding-plane faces with a careful arrangement of the cells in the direction normal to the

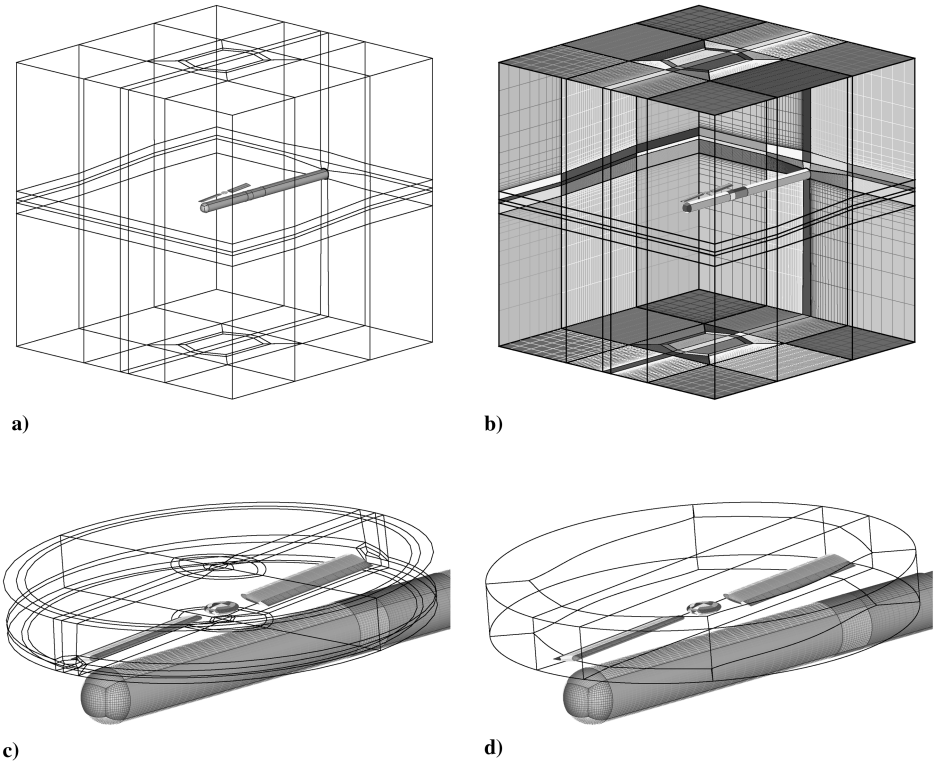

Fig. 4 Georgia Tech test case with the two-bladed teetering rotor mounted above an idealized airframe with cylindrical shape: a) boundary surface and block boundaries, b) surface mesh, c) rotor grid outer surface forming a cylindrical drum, and d) rotor mesh placed within a matching drum-shaped cavity in the background mesh.

Table 1 Summary of conditions for the generic rotor–fuselage cases

		Test conditions			Blade pitch			Multiblock mesh	
Test case	Model	μ	M_{tip}	θ_{shaft}	θ_0, deg	θ_{1s}, deg	θ_{1c}, deg	Blocks	Cells
Georgia Tech	Euler, no flapping	0.10	0.295	6.0	10	0.0	0.0	514	2.5×10^6
Georgia Tech	Euler, flapping	0.10	0.295	4.0	10	2.0	−2.0	514	2.5×10^6
Georgia Tech	RANS, flapping	0.10	0.295	4.0	10	2.0	−2.0	514	9.8×10^6
ROBIN	Euler	0.15	0.50	3.0	6.5	2.2	−2.0	696	9.6×10^6

sliding plane. A further consideration is related to the trim state of the rotor, in which excessive flapping combined with elastic blade deflection at the tip will need a relatively large rotor drum to be accommodated. To alleviate this problem, the pitch-flap equivalence can be used to restrict the flapping motion and confine the blade in a smaller drum. This induces a change in the shaft angle as well. Regardless of this limitation, the method can be used for quite complex cases, as demonstrated in Fig. 3 for a realistic helicopter configuration.

IV. Georgia Tech Teetering-Rotor Test Case

The first rotor–fuselage test case considered in this work is based on the experiments conducted at Georgia Institute of Technology for an idealized fuselage interacting with a two-bladed teetering rotor [5]. For this test case, unsteady surface pressure measurements as well as particle-image velocimetry data are available. This availability and the low geometric complexity of the considered wind-tunnel model make this a well-established test case for investigations of interactional aerodynamics and validation of CFD codes. The configuration consists of a 134-mm-diam cylindrical airframe with a hemispherical nose. It is supported by a wind-tunnel sting, independent of the two-bladed rotor that is driven by a shaft mounted on the wind-tunnel ceiling. In the present work, the wind-tunnel support for the airframe and the rotor drive shaft are neglected. Figures 4a and 4b show the idealized geometry considered in the present investigation. The rotor center was located 1.0 rotor radius behind the center of the hemispherical nose cone and $0.3R$ above the centerline of the airframe. The rotor is of the teetering type and the blades are untwisted with NACA0015 sections. The blade chord was 86 mm and the radius was 450 mm. The conditions as well as the details of the computational meshes used are presented in Table 1. The test case has an advance ratio of 0.10, leading to $C_T = 0.0090$. The rotor was mounted at a 6 deg forward shaft tilt. The effect of viscosity is analyzed by comparing results from simulations based on the Euler equations with those based on the Navier–Stokes equations. The grids employed for the inviscid simulations, as well as the finer meshes used for the viscous simulations, have a total of 514 blocks. The rotor grids have a C-H topology and 324 blocks, and the background grid containing the airframe has 190 blocks with an O-type topology around the cylindrical airframe. For viscous computations, the entire domain (rotor and fuselage) was modeled as fully turbulent flow. The grid density was selected based on previous experience with rotor flows [31]. The fuselage grid was based on previous efforts with the isolated ROBIN body [4]. The current grids are finer than those previously used and, of course, limited by the available CPU resources. Although grid convergence was not explicitly investigated, preliminary calculations with coarser grids suggest that no substantial deficiencies are due to the employed grid density, at least for the Georgia Tech and the ROBIN test cases. The details of the grids are given in Table 1. The azimuthal time step was set to 1 deg, again based on previous experience. In the simulations, the one-piece rotor from the experiment was replaced by a rotor with a small root cutout and a simple ellipsoidal rotor head. The far-field boundaries considered in the simulations were formed by a rectangular box. The rotor grid has flat upper and lower boundaries and a cylindrical outer boundary surface. This mesh was embedded in a cylindrical drum-shaped cavity in the stationary airframe grid. The sliding-plane method was employed on the drum-shaped surface surrounding the rotor grid, as sketched in Figs. 4c and 4d. The surface mesh for the airframe and rotor is also shown in Fig. 4. In the present simulations, the first flap harmonic of the rotor was replaced by a cyclic pitch motion and modified rotor shaft inclination, using the pitch-flapping equivalence. The flapping coefficients were obtain from published works [16]. The motivation behind the removal of the flapping motion is that the close proximity of the rotor and the cylinder for $\psi = 180$ deg (i.e., at the front of the rotor disk) leads to a rotor grid with a lower domain boundary close to the rotor plane. The flapping motion would therefore have given a more significant grid deformation than the equivalent pitching motion.

The chordwise surface pressure distribution for the rotor from the inviscid simulations with and without flapping were compared in a previous work [32], showing that the effect of the flapping of the rotor is to increase the effective blade incidence at the retreating side and the rear part of the rotor disk. The figures also indicate that the rotor has subsonic flow even at the most outboard stations of the advancing side, due to the low tip Mach number of 0.295, combined with the moderate advance ratio of 0.10.

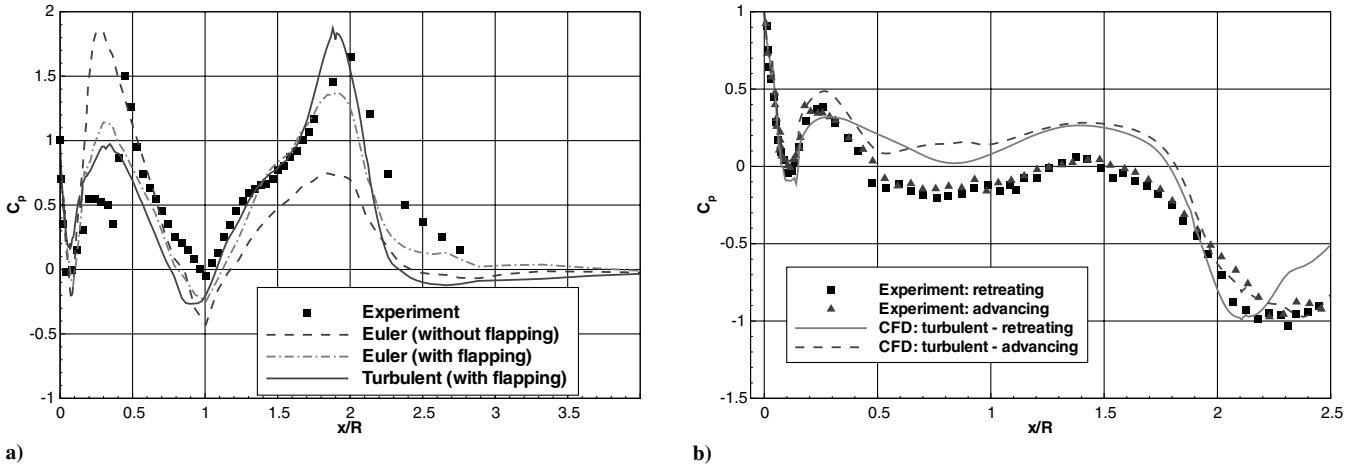

Fig. 5 Georgia Tech test case ($\mu = 0.10$ and $C_T = 0.0090$) with time-averaged pressure on the cylinder: a) $y = 0$, upper surface (crown line) and b) $z = 0$; retreating side (left) and advancing side (right).

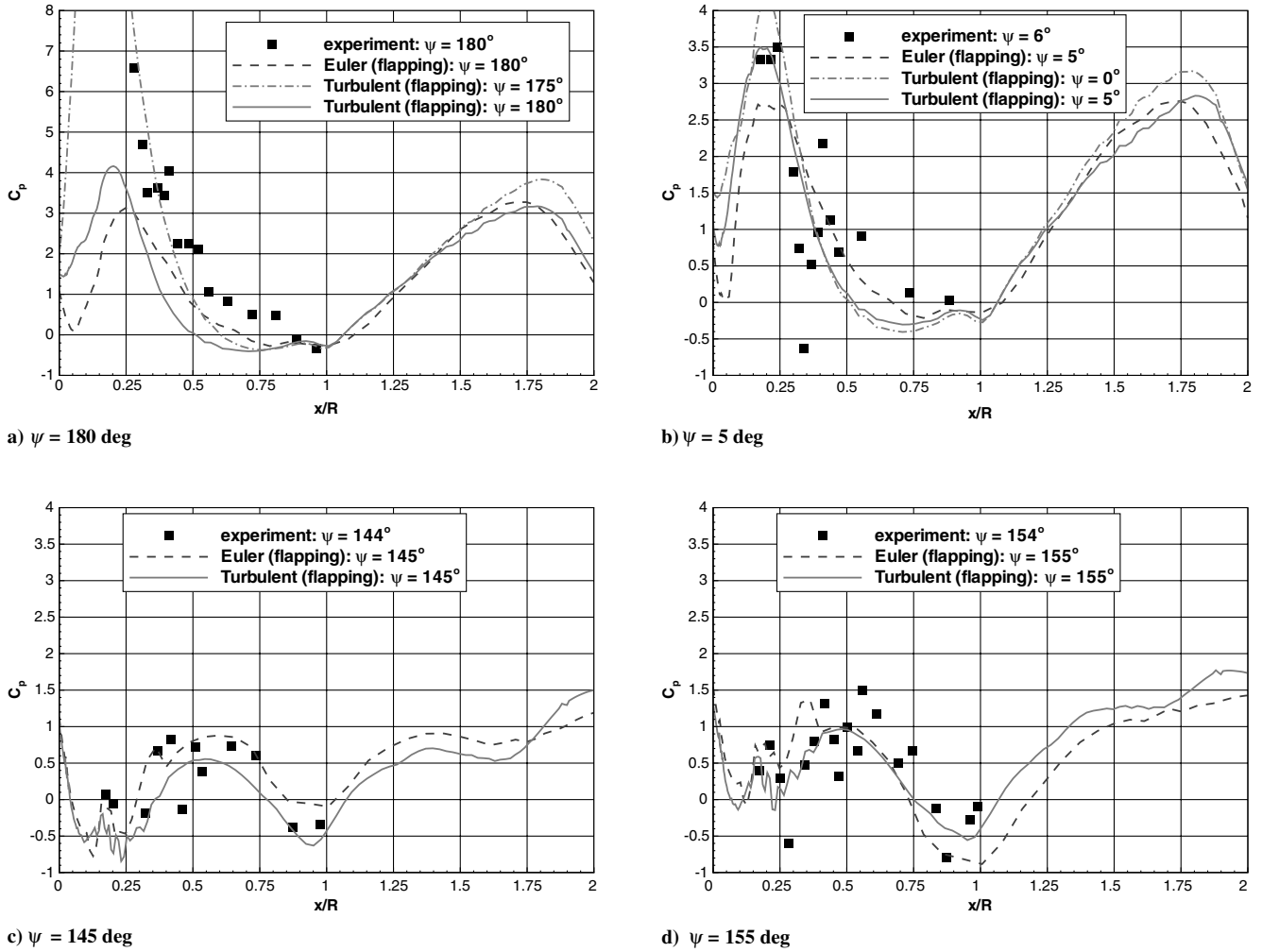

a) ψ = 180 deg

b) ψ = 5 deg

c) ψ = 145 deg

d) ψ = 155 deg

Fig. 6 Georgia Tech test case ($\mu = 0.10$ and $C_T = 0.0090$); instantaneous pressure along the crown line of the cylindrical body for different rotor azimuths.

The first rotor–fuselage interactional aerodynamic effect considered here is the change in the time-averaged pressure distribution along the crown line of the cylinder compared with the steady state pressure without the rotor. In Fig. 5a, the time-averaged pressure along the crown line of the model from three simulations is compared with experimental data. To investigate the sensitivity of the result with respect to the employed flapping schedule, two inviscid simulations on a relatively coarse mesh were performed: with and without flapping. In addition, results from a turbulent Navier–Stokes simulation on a finer mesh are presented. The viscous simulation employed the same flapping schedule as the inviscid flapping case. For this untwisted rotor, most of the load is carried outboard. The stagnation of the induced-velocity component normal to the cylinder surface gives rise to a pressure increase, forming peaks in the time-averaged pressures near $x/R = 0$ and 2. These peaks are captured well in the present simulations, compared with the experimental data. The Euler simulations obviously do not include the effects of the viscous interaction of the vortex wake of the rotor with the boundary layer on the cylinder. Also, the experimental data indicate that the flow will have separation in the nose region (where the c_p has a plateau between $x/R = 0.2$ and 0.4) through at least part of the rotor revolution, an effect absent from the simulations. Figure 5a also shows the effect of the flapping on the cylinder surface pressure. Consistent with the increased rotor loading on the advancing side and rear part of the rotor disk, increased rear loading near the second peak is observed, whereas reduced loading occurs at the front of the disk. A comparison of the inviscid and turbulent cases with the same flapping schedule shows that the addition of viscous effects reduces the pressure increase at the front of the model, whereas the peak of the back of the rotor disk increases. As mentioned in Sec. II, the predictions based on the Euler equations by both Hariharan and Sankar [23] and Park and Kwon [16] underpredict the peak of the averaged pressure present at the back of the rotor disk relative to the experimental data. The present comparison shows that the absence of viscous effects can at least partly explain this discrepancy. The results of O'Brien [27] obtained using an actuator-blade model implemented in an incompressible Navier–Stokes simulation method showed a good agreement with the experiment, as a further indication that viscous effects play an important role in this test case. For the

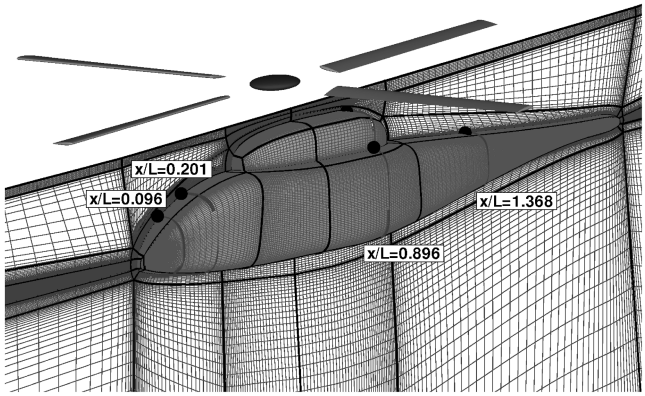

Fig. 7 ROBIN configuration used in the present CFD study. The wind-tunnel supports for the floor-mounted fuselage and the roof-mounted rotor are omitted. Shown is the fuselage and symmetry plane mesh, with the sliding plane located 1.0 blade chord below the rotor disk as well as the location of pressure taps used in the present work.

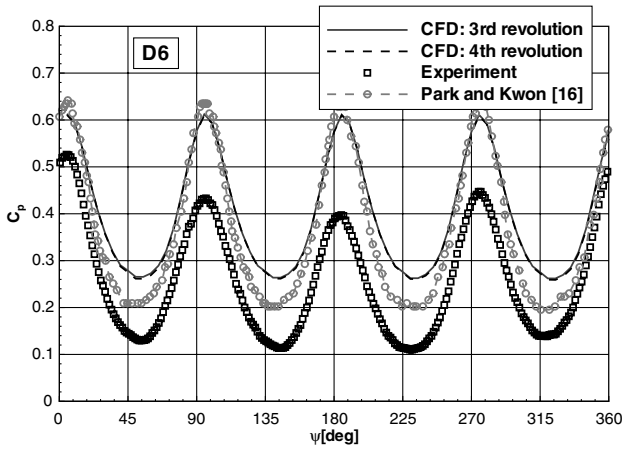

a) Centerline, $x/L = 0.096$

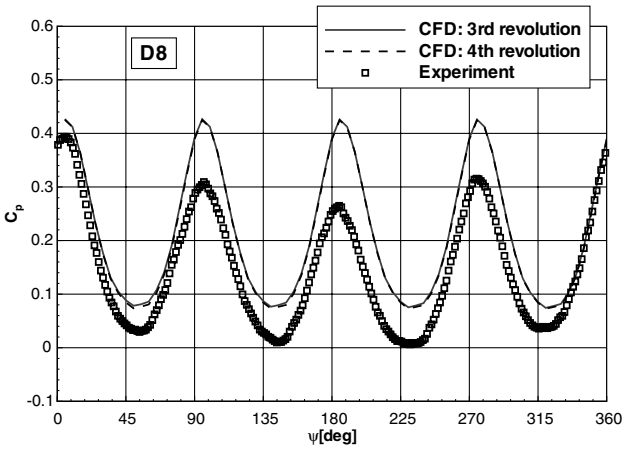

b) Centerline, $x/L = 0.201$

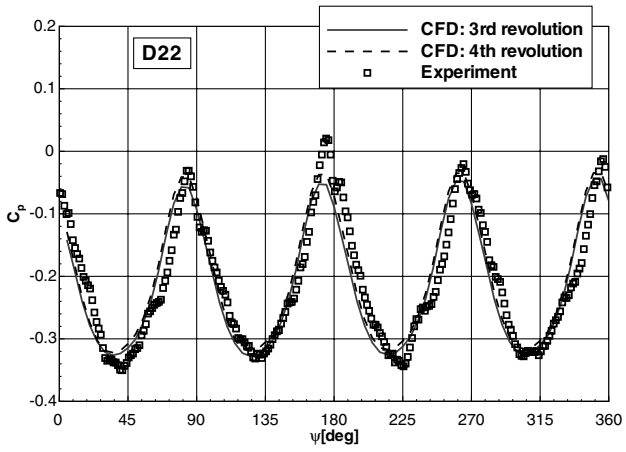

c) Centerline, $x/L = 0.896$

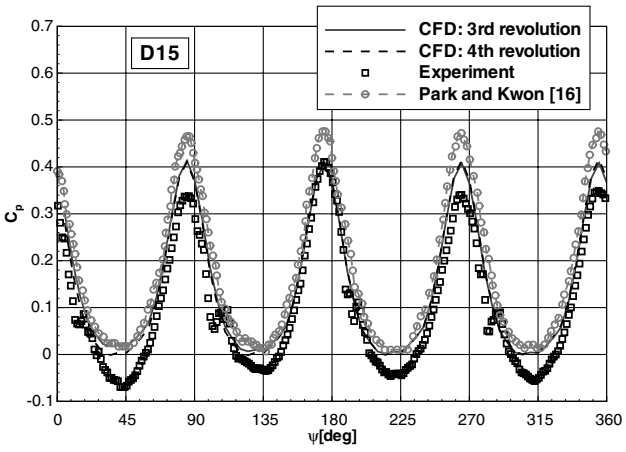

d) Centerline, $x/L = 1.368$

Fig. 8 ROBIN rotor–fuselage test case ($\mu = 0.15$). centerline surface pressure distribution for the ROBIN test case.

present set of viscous results, the standard k-ω model was used in a fully turbulent fashion. Perhaps this model is not the most sensitive to rapid changes of pressure gradient and the separation is underpredicted. As can be seen in Fig. 5a, the viscous pressure curve shows a change of slope near the $0.25\,x/R$ station. This at least shows that viscous model can capture some of the phenomena observed during the experiment.

Figure 5b shows the time-averaged pressure along the left and right $z = 0$ lines for the viscous simulations compared with the experimental data. Again, the overall pattern is well resolved, and the absence of the rotor head and support could at least partly explain some of the discrepancies around and downstream of the $x/R = 1$ station.

The instantaneous surface pressure along the crown of the cylinder is shown in Fig. 6. The figure compares the Euler and Navier–Stokes results including the blade flapping with experimental data. Figures 6a and 6b show the situation when the blade is passing over the nose of the cylinder for blade azimuths of 180 and 185 deg, respectively. The viscous simulation well resolves the sharp rise of surface pressure. The pressure increase due to the rotor-induced flow

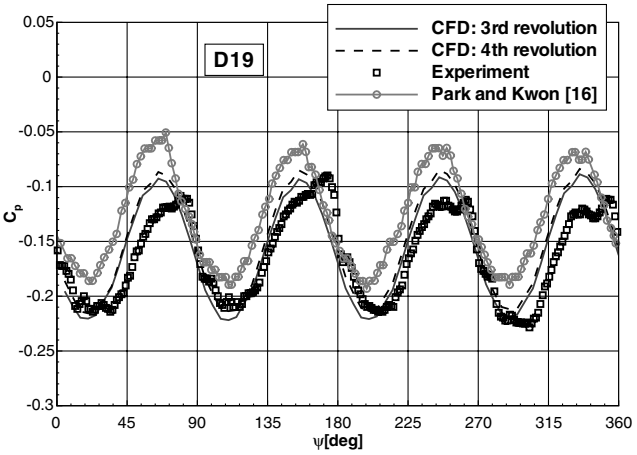

a) $x/L = 0.896$, $y/L = -0.07$, $z/L = 0.125$

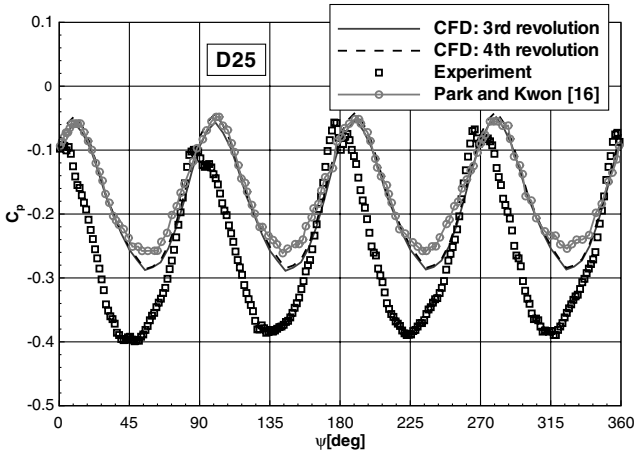

b) $x/L = 1.368$, $y/L = 0.07$, $z/L = 0.125$

Fig. 9 ROBIN rotor–fuselage test case ($\mu = 0.15$). Surface pressure in probes left and right of the fuselage fairing for the ROBIN test case.

far exceeds the stagnation pressure of the freestream flow. The plots also show the strong azimuthal dependency of the instantaneous pressure, which means that a slight shift in phasing relative to the experimental data could lead to substantial discrepancies with the experiment. Figure 6c and 6d shows the pressure at blade azimuth angles of 145 and 155 deg, respectively. These correspond to 35 and 25 deg of azimuth before the blade passage. Clearly, the induced pressures are significantly lower than before, because no direct interaction with the blade occurs.

V. ROBIN Test Case

A second test case considered in this paper involves the ROBIN helicopter model [9,12,13]. The overall configuration is shown in Fig. 7. The four-bladed rotor has an aspect ratio of 13 and consists of a NACA0012 section, with a linear twist of 8 deg In the experimental setup, the rotor was suspended from the wind-tunnel roof, and the fuselage was on a floor-mounted support. Both supporting structures are omitted in the geometry used here. The rotor hub is modeled as an ellipsoidal surface. The CFD geometry includes the 2 in. rotor shaft offset from the fuselage centerline and the 3 deg forward tilt of the rotor shaft. Figure 7 also shows the locations of the surface pressure taps and inflow flow measurements from the NASA experiments, which are used here. The test case considered had a rotor tip Mach number of 0.5, the advance ratio was 0.15, and the rotor thrust coefficient was $C_T/\sigma = 0.0656$, as in the experiment. The conditions as well as the rotor trim state are summarized in Table 1. The rotor trim state was obtained from published work by Park et al. [15]. The inviscid flow simulations were conducted on multiblock structured grids with the sliding-plane interface located one blade chord below the rotor disk. The grid had an O-type topology in the direct vicinity of the fuselage, embedded in a domain with a cylindrical side surface, of the same diameter as the rotor grid far-field boundary, and an upper surface orthogonal to the rotor shaft. The grid was made of 240 blocks and 4.0×10^6 cells. The rotor grid had a C-H topology, with 456 blocks and 5.5×10^6 cells. The grid had 50 cells in the spanwise direction of each blade, 45 cells in the surface normal direction, 150 cells around the blade chord, and 40 cells in the streamwise direction between the blades. The simulation was run for four rotor revolutions using azimuthal steps of 1.0 deg. For the fourth rotor revolution, the thrust coefficient was $C_T/\sigma = 0.0066$, which is within 0.6% of the value for the third revolution, indicating a sufficient level of convergence, confirmed by surface pressure plots for the third and fourth revolutions discussed later. The searches and interpolation weights for the sliding meshes were precomputed as discussed in [2], requiring about 5% of the total CPU time. The sliding-plane method added an additional 5–6% communication overhead for the parallel simulation conducted on 40 Pentium 4 processors of a Linux cluster.

An important step in the validation of the present sliding-plane method was a comparison of the computed time-averaged induced flowfield components in the streamwise and rotor-disk normal directions with the experimental data [10]. The comparison was published previously [2] and showed a favorable agreement, with a slight overprediction of the streamwise component. This was an encouraging result, because any loss of continuity across the sliding plane would have an effect on the obtained velocity field.

Time-averaged surface pressure coefficients were compared with experimental data in previous work [2], showing a good agreement, with small discrepancies at the lower side of the model that can be (partly) attributed to the absence of the wind-tunnel support in the CFD geometry.

Figures 8 and 9 compare the predicted time-dependent surface pressure coefficients with the experimental data [13]. The pressure at the four centerline positions defined in Fig. 7 is shown in Figs. 8a–8d. One can see that the two numerical solutions compared in the figure show a well-established periodic pressure signal. This is not exactly the case with the experiment, in which each blade seems to have a slightly different effect on the surface pressure. Interestingly, the first peak of the period is very well captured both in phase and magnitude for sensor D8, whereas this is not the case for sensor D6, which is located closer to the nose of the fuselage. For this first sensor, an offset appears to be present, which could be due to viscous or transitional flow effects that are not captured by either of the inviscid CFD simulations compared. Again, the peak-to-peak variation of the surface pressure coefficient is not far from the experimental values. Part of this offset could be due to the employed trim state, which has a stronger effect near the tip of the blade. The present trim state is an estimate and selected to agree with the work of Park and Kwon [16] and Nam et al. [17]. Further downstream, the agreement between CFD and experiments is much better, with the CFD capturing both phase and magnitude of the surface pressure variation. As was the case before, the CFD results appear to be more periodic than the experiment, which now shows slightly higher values for the third blade passage, at least for sensor D22. Sensor D25 also compares well, considering its location downstream of the rotor hub on the fuselage fairing. The pressure at probe locations on the side of the fuselage fairing is shown in Figs. 9a and 9b for the retreating and advancing sides of the rotor, respectively. The peak-to-peak pressure fluctuations agree favorably with the experiment and the results of

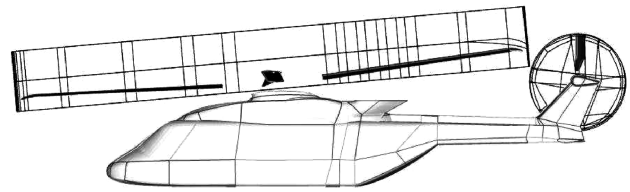

a)

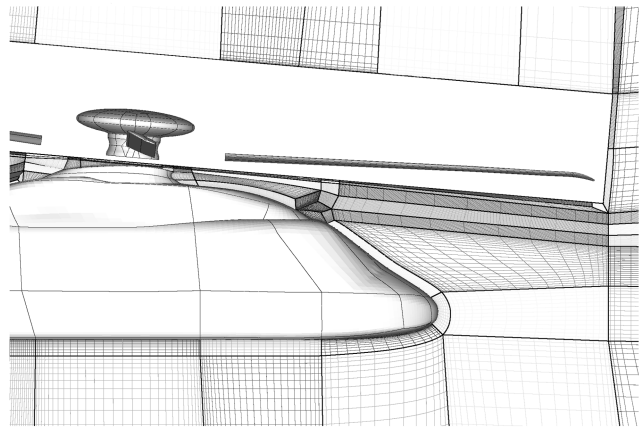

b)

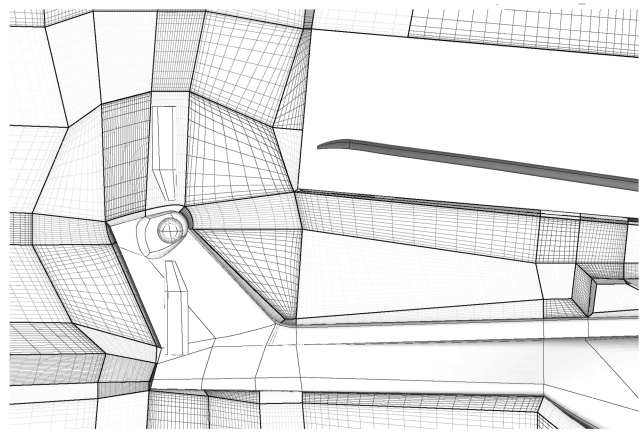

c)

Fig. 10 GOAHEAD full-helicopter geometry: a) main and tail rotors are placed within drum-shaped sliding-plane interfaces and b–c) mesh in the $y = 0$ plane, which does not constitute a symmetry plane. The rotor meshes are not shown, for clarity. The mesh has 3786 blocks and 27.8×10^6 cells.

Park et al. [15], which are shown here for comparison. Sensor D19 shows some improvement in comparison with previous published results, though an offset still exists between the CFD and the experiment. This could be due to viscous effects, the rotor support (which is not present in the CFD), and differences in the rotor hub (which was represented by a small disk in computations).

VI. GOAHEAD Rotor–Fuselage Test Case

A second rotor–fuselage test case demonstrates the capability of the method to handle complex, realistic helicopter geometries. The case considered here is the wind-tunnel model of a medium-weight generic helicopter with the four-bladed ONERA 7AD rotor, equipped with anhedral tips and parabolic taper, and the BO105 two-bladed tail rotor. This configuration is under investigation for the GOAHEAD European Commission 6th Framework Research Project. Figure 10 shows the geometry and the multiblock structured mesh used for the Reynolds-averaged Navier–Stokes simulations. For this full-helicopter geometry, the main and tail rotors are placed within a drum-shaped sliding-plane interface, as shown in Fig. 10a. The close proximity of the main and tail rotor planes is notable in the figure, which leads to an additional challenge in the generation of the multiblock structured meshes used here. The main rotor drum has the forward tilt of the main rotor shaft, and the tail rotor drum is tilted about the x axis as well as the z axis (in the tail rotor hub-centered coordinate system) to provide a small forward and upward thrust component. The multiblock mesh used here consists of 3786 blocks and approximately 27.8×10^6 cells. The mesh in the $y = 0$ plane is shown in Figs. 10b and 10c. The computed case corresponds to an economic cruise condition, for which the freestream Mach number is 0.204 and the tip Mach number of the rotor 0.62. A representative rotor trim schedule is used in the simulation; that is, the rotor has cyclic pitch change as well as a harmonic blade flapping. The multiblock topology of the rotors is designed to handle the grid deformation as discussed in [1]. This test case was run on the Hector supercomputer at the Edinburgh Parallel Computing Centre in Edinburgh. The simulation was run for three rotor revolutions with a time step corresponding to 0.25 deg of main rotor rotation. The tail rotor was rotating five times faster and consequently, steps of 1.25 deg were used. The k-ω turbulence model was used and the whole domain was modeled as a fully turbulent, viscous flow.

Figure 11a shows the instantaneous surface pressure distribution at a main rotor azimuth of 90 deg during the third revolution (economic cruise conditions, $\mu = 0.3$). The effect of the blade passing on the surface pressure distribution on the front part of the fuselage is shown in detail in Fig. 11b, in which the $x = 0.75$ plane is shown. The main rotor blade passing through the front of the rotor disk clearly induces a (delayed) pressure rise on the forward fuselage, as discussed previously in [2]. The interaction of the tail rotor with the fin is shown in Fig. 8c, showing the c_p contours in the $z = 0.775$ cross section. The tail rotor blade is at $\psi = 0$ deg, which corresponds to the downward vertical position. For the rotation direction of the tail rotor used here, this position is on the retreating side of the tail rotor disk. The blade stagnation pressure in the selected cross section is therefore only around twice the fin stagnation pressure. In addition to the direct impulsive effect, the tail-rotor–fin interaction also includes the effect of the tail rotor induced velocity on the flow around the side-force-generating fin by effectively changing the flow angle in a time-periodic fashion. This effect is more difficult to analyze than the pressure impulse effect shown in the figure. A comparison of simulation results with and without tail rotor would clearly show this contribution.

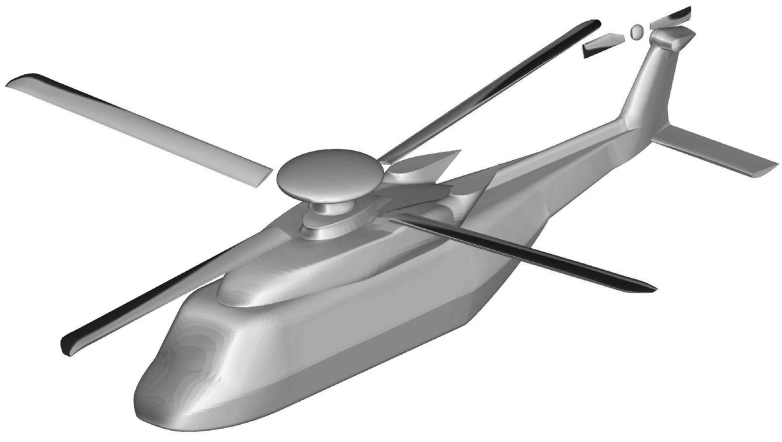

a)

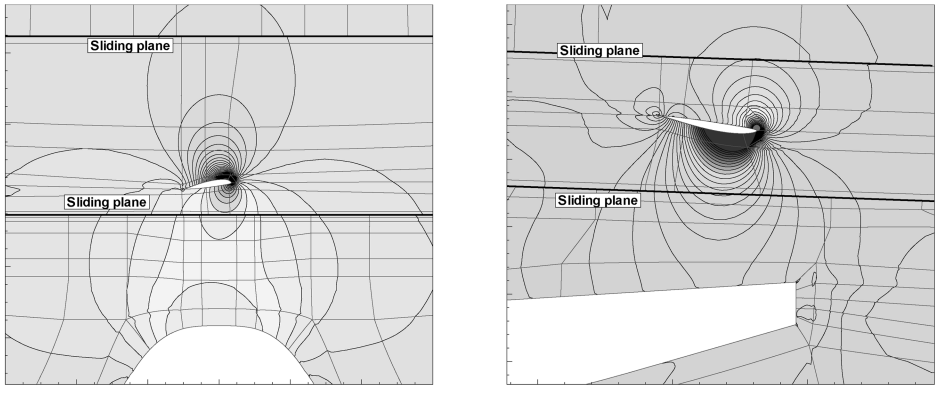

b) c)

Fig. 11 GOAHEAD full-helicopter geometry. Economic cruise condition. Instantaneous pressure coefficients are shown: a) instantaneous surface pressure coefficient at main rotor azimuth of 90 deg; b) main-rotor–fuselage interaction, $x = 0.75$ cross section (approximate midspan of the blade); and c) tail-rotor–fin interaction, $z = 0.775$ cross section, at the base of the fin.

Figure 12 shows a comparison of the rotor-disk loading for the full helicopter with that from the isolated rotor. In the figures, the rotor rotates clockwise and the direction of travel of the rotor is from right to left.

Figure 12a shows the sectional normal force coefficient as a function of blade radial station and blade azimuth. Here, the normal force coefficient is based on the freestream Mach number. The difference between the two results is shown in Fig. 12b. From the two plots, a number of observations can be made regarding the effect of the fuselage and fin–tail-rotor assembly on the main rotor loading. First, the interactional effect is mostly restricted to the front and rear of the disk; that is, the advancing side as well as the retreating side loading do not change significantly due to the presence of the helicopter fuselage. Second, the fuselage induces an upwash, which effectively increases the blade angle of attack through a significant area at the front of the rotor disk. In a similar vein, the fuselage creates downwash behind the fairing, which leads to a reduction of the blade angle of attack for parts of the rear of the rotor disk. Compared with the upwash area at the front of the disk, the extend of the downwash area at the rear of the disk appears to be smaller. In particular, at the front of the rotor disk, the interactional effect extends to blade stations further outboard, as compared with the interaction at the rear of the rotor disk. The apparent stronger inflow angle changes at the front of the rotor disk can, at least partly, be explained by the effect of the forward tilt of the rotor shaft. At the front of the disk, the blade passes significantly closer over the fuselage than at the back of the helicopter, as can be seen from Fig. 10. The observed increased blade loading at the front of the rotor disk is consistent with the results of Potsdam et al. [26] for the UH-60A helicopter, and the reduced blade loading at inboard stations at the back of the rotor disk is consistent with the Dauphin 365N result of Sides et al. [14]. In contrast to these works, the results presented in Fig. 12 clearly demonstrate the radial and azimuthal extents of the fuselage-induced upwash/downwash. Assuming that the blade loading in each section is predominantly a function of the local dynamic head as well as the local sectional angle of attack, the present results can be used to estimate the change in the blade angle of attack due to the changes in the induced flow as a result of the fuselage blockage. Figure 12c shows the difference in the sectional normal force coefficient based on the local dynamic head between the full-helicopter and the isolated rotor results. Assuming quasi-steady attached flow and neglecting three-dimensional effects, this normal force coefficient is a direct measure of the effective angle of attack at any given blade station. The reversed-flow region and its immediate vicinity are excluded in Fig. 12c, because the quasi-steady attached-flow assumption is invalid in this region. The differences in normal force coefficient shown in Fig. 12c can be used to determine the effective angle-of-attack changes; that is, the changes in angle of attack can be obtained by dividing the normal force coefficient

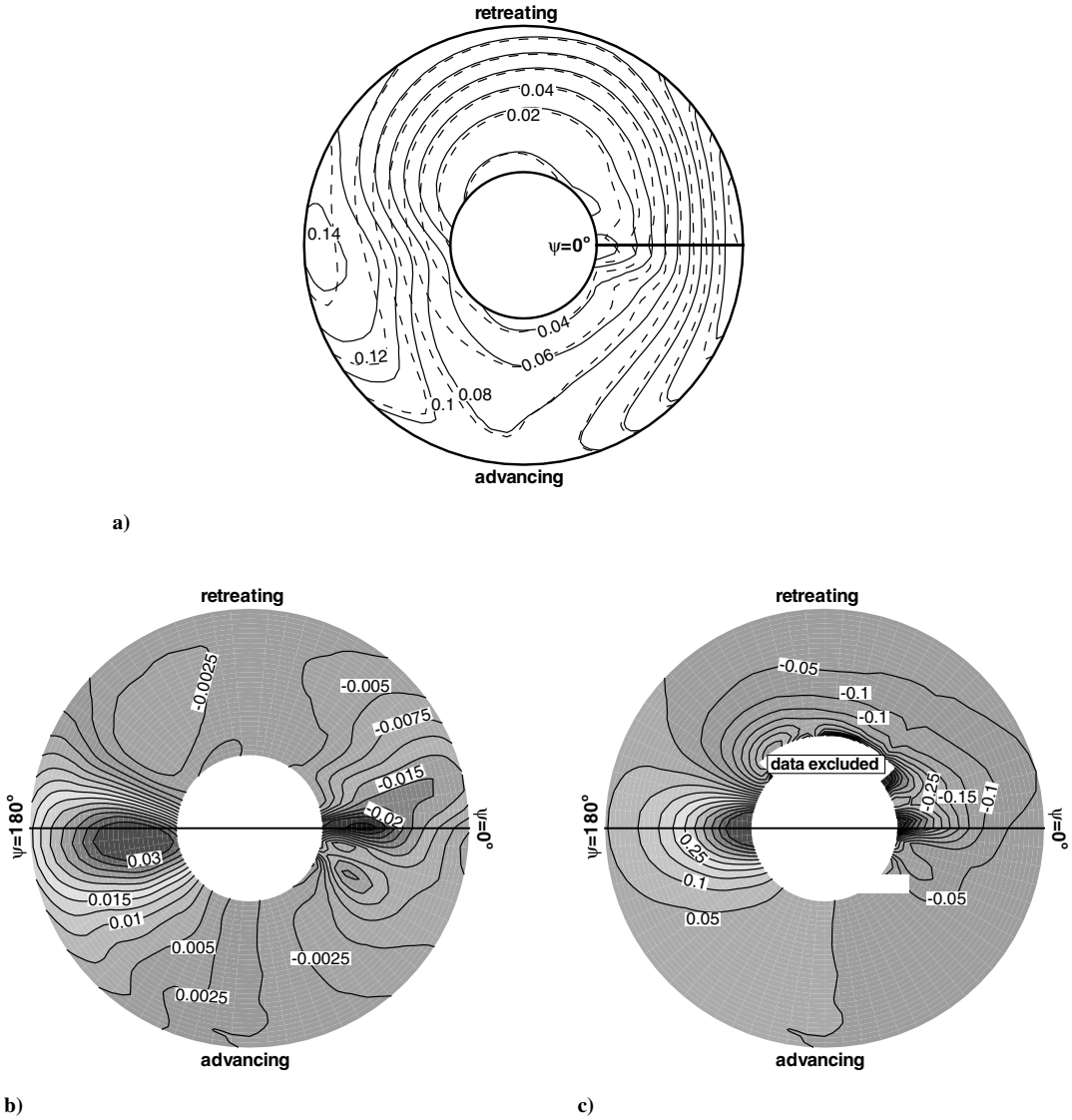

Fig. 12 Effect of fuselage on rotor loading for the GOAHEAD economic cruise case: a) M^2c_n distribution over the rotor disk for full helicopter (solid) and isolated rotor (dashed), b) change in M^2c_n distribution due to the presence of the fuselage and tail rotor (full helicopter minus the isolated rotor values), and c) change in C_n force coefficient based on local dynamic head.

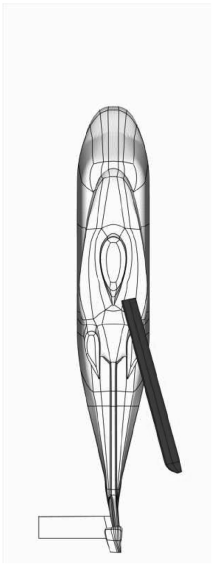
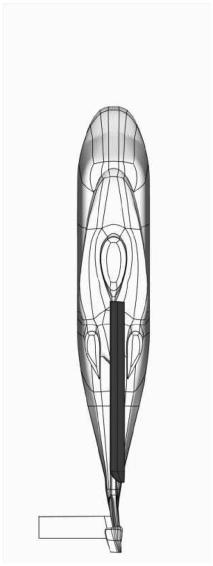
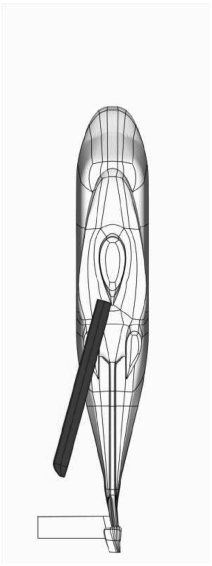

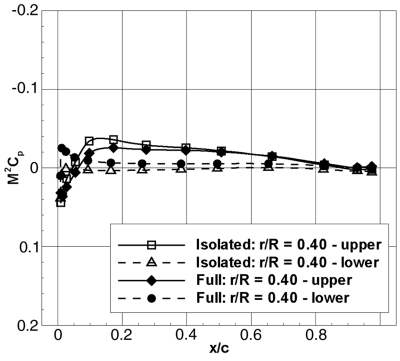

a) $r/R = 0.4$

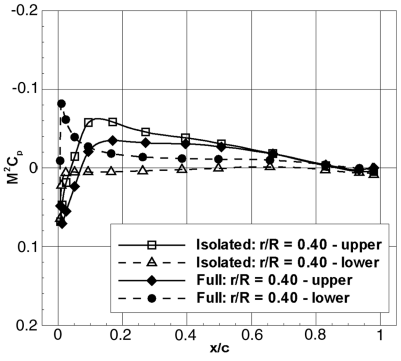

d) $r/R = 0.4$

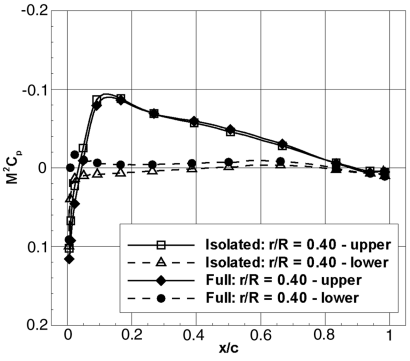

g) $r/R = 0.4$

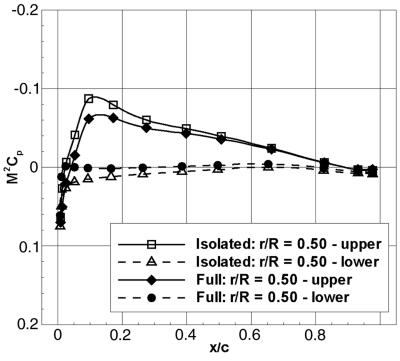

b) $r/R = 0.5$

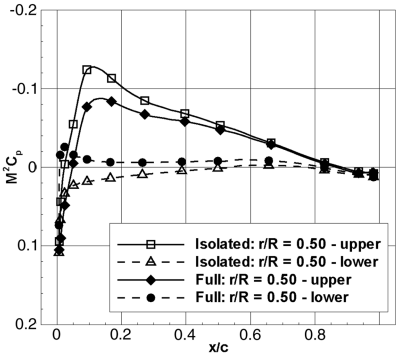

e) $r/R = 0.5$

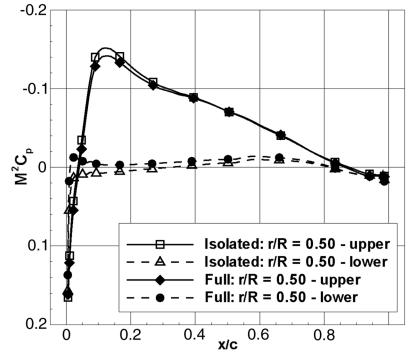

h) $r/R = 0.5$

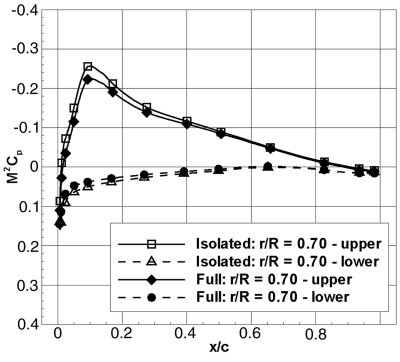

c) $r/R = 0.7$

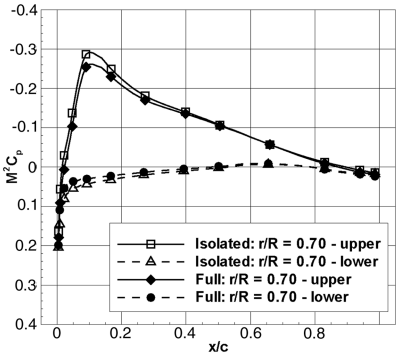

f) $r/R = 0.7$

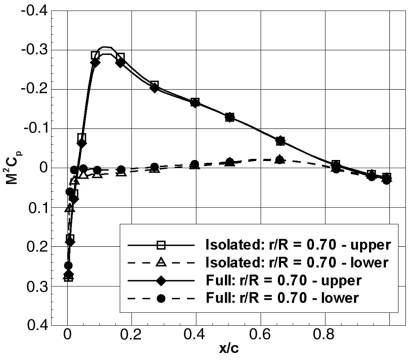

i) $r/R = 0.7$

Fig. 13 GOAHEAD economic cruise; fuselage effect on rotor loading; rear of the rotor disk.

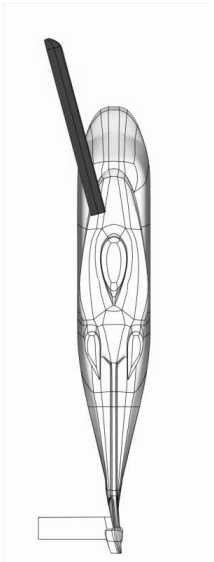
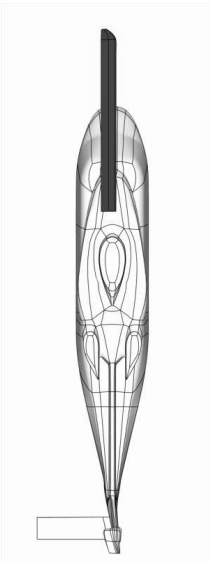
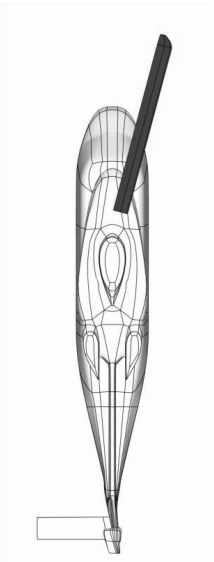

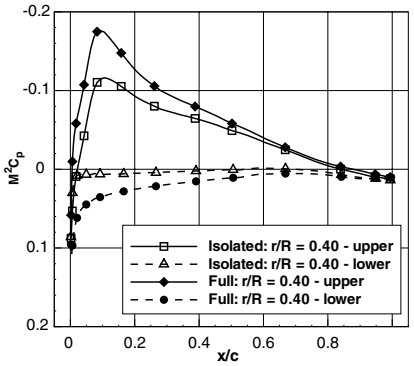

a) $r/R = 0.4$

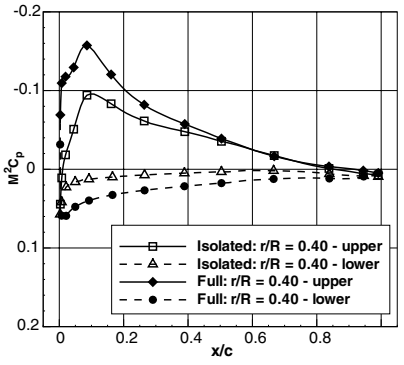

d) $r/R = 0.4$

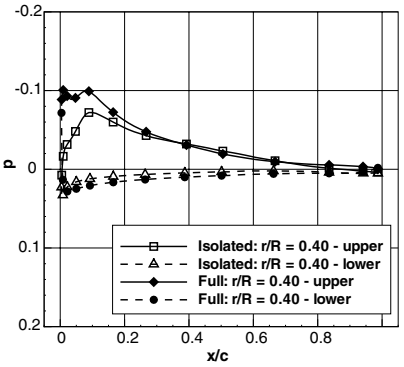

g) $r/R = 0.4$

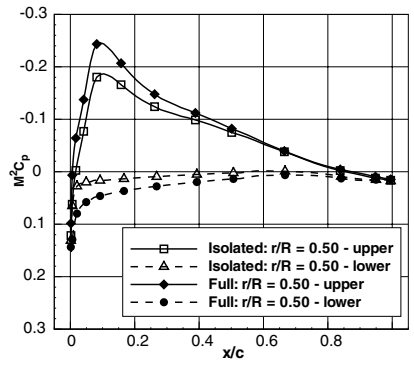

b) $r/R = 0.5$

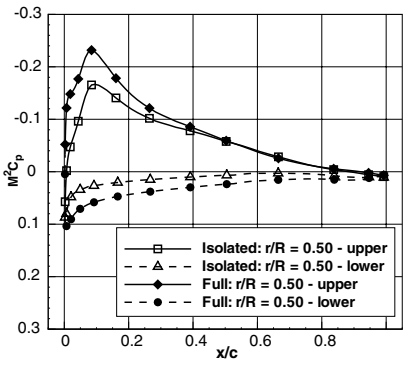

e) $r/R = 0.5$

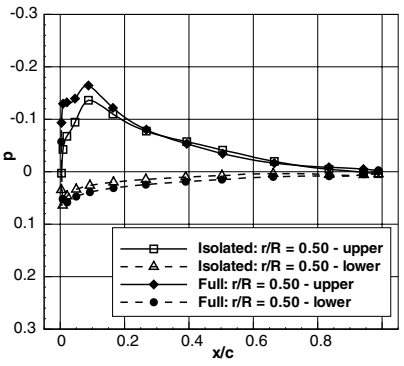

h) $r/R = 0.5$

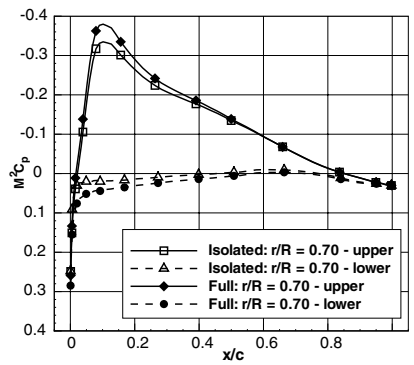

c) $r/R = 0.7$

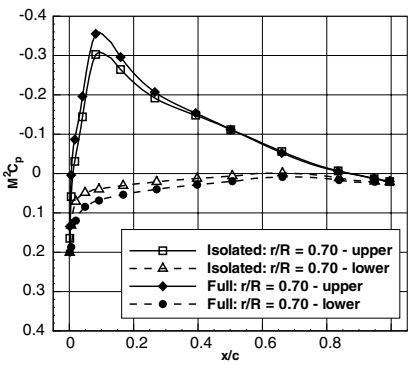

f) $r/R = 0.7$

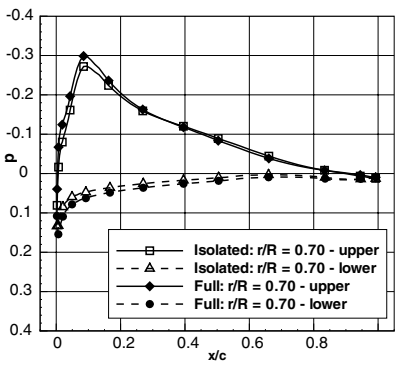

i) $r/R = 0.7$

Fig. 14 GOAHEAD economic cruise; fuselage effect on rotor loading; front of the rotor disk.

changes with the lift-curve slope at the particular angle of attack and Mach number component in the chordwise direction. The quasi-steady angle-of-attack changes are in the range of 2–3 deg at the inboard part of the blade at both the front and rear of the rotor disk. Interestingly, at the front of the rotor disk, the maximum blade normal force changes due to the rotor–fuselage interaction arise ahead of the $\psi = 180$ deg position (i.e., before the blade passes over the fuselage centerline), as shown in Fig. 12b. The region with significant flow-angle changes at the front of the rotor disk due to the rotor–fuselage interaction is more centered around the fuselage centerline (i.e., the $\psi = 180$ deg azimuthal position).

Figure 13 shows the chordwise surface pressure coefficients in the $r/R = 0.4$, 0.5, and 0.7 blade sections for three blade azimuths at the rear of the rotor disk. In the figures, the lines with open symbols correspond to the isolated rotor results and solid symbols are used for the full-helicopter simulation. The changes in the surface pressure can be interpreted as an effective change in local angle of attack, the stagnation-point location, and the pressure-side surface pressure distribution constitute an effective indicator for the angle-of-attack changes. For the rear of the disk, the interactional effect is largely restricted to the inboard 50% of the blade. Figure 14 shows the same comparison for three azimuthal stations at the front of the disk. It can be seen that significant interactional effects are present at up to 70% of the blade radius around the $\psi = 180$ deg azimuthal position. Interestingly, at the 70% radial station, the differences at the front of the disk appear larger than at the same stations at the rear of the disk, shown in Fig. 13. As mentioned earlier, the closer blade–fuselage spacing at the blade passage over the front of the disk, compared with the blade passage over the rear of the fuselage, can be partly attributed to this effect. Furthermore, for the condition considered, the blade pitch and flap schedules in the used trim state give rise to larger blade incidence angles at the back of the rotor disk (around $\psi = 0$ deg) than at the front of the rotor disk (i.e., around $\psi = 180$ deg). Therefore, at the back of the rotor disk, the relative blade loading changes can be expected to be smaller.

VII. Conclusions

A computational analysis of helicopter interactional aerodynamics has been performed using the HMB CFD method, which has been extended with a sliding-mesh algorithm enabling simulations of flows around full-helicopter configurations. A comparison of the results obtained using the HMB method with experimental data shows that the method is capable of resolving the main interactional flow features for the generic cases. A similar comparison for the GOAHEAD test case has not yet been conducted, but is planned for the near future in the framework of the European Commission Framework 6 GOAHEAD project. The results obtained for the GOAHEAD test case show the capability of the CFD method to handle flow simulations for complex helicopter configurations in demanding flight conditions. In addition, the influence of the helicopter fuselage on the rotor loads has been investigated by comparison of the loads from a full-helicopter simulation with the results from an equivalent isolated rotor simulation. The results highlight the interactional effect on the sectional loads as a function of both the blade azimuthal position and the radial position on the blade. Substantial differences were observed inboard of the 70% station, especially near the front of the rotor disk. The present results show rapid changes as a function of blade azimuth for the interactional effect on the rotor loads, which complicates the formulation of a simple correction for the fuselage effect on the rotor loads. However, some of the effect can be captured by prescribing changes in the blade incidence near the front and rear of the rotor disk.

Acknowledgments

During this work, R. Steijl was supported by the European Commission under the Integrating and Strengthening the European Research Area Programme of the 6th Framework, contract no. 516074 [Generation of Advanced Helicopter Experimental Aerodynamic Database (GOAHEAD) project]. Some of the computations presented in this paper were carried out using the Hector supercomputer of the United Kingdom under the Engineering and Physical Sciences Research Council grant EP/F005954/1.

References

[1] Steijl, R., Barakos, G., and Badcock, K., "A Framework for CFD Analysis of Helicopter Rotors in Hover and Forward Flight," *International Journal for Numerical Methods in Fluids*, Vol. 51, No. 8, 2006, pp. 819–847. doi:10.1002/fld.1086

[2] Steijl, R., and Barakos, G., "Sliding Mesh Algorithm for CFD Analysis of Helicopter Rotor-Fuselage Aerodynamics," *International Journal for Numerical Methods in Fluids*, Vol. 58, No. 5, 2008, pp. 527–549. doi:10.1002/fld.1757

[3] Badcock, K., Richards, B., and Woodgate, M., "Elements of Computational Fluid Dynamics on Block Structured Grids Using Implicit Solvers," *Progress in Aerospace Sciences*, Vol. 36, Nos. 5–6, 2000, pp. 351–392. doi:10.1016/S0376-0421(00)00005-1

[4] Barakos, G., Steijl, R., Badcock, K., and Brocklehurst, A., "Development of CFD Capability for Full Helicopter Engineering Analysis," 31st European Rotorcraft Forum, Florence, Italy, Council of European Aerospace Societies Paper 91, 2005.

[5] Brand, A., McMahon, H., and Komerath, N., "Surface Pressure Measurements on a Body Subject to Vortex Wake Interaction," *AIAA Journal*, Vol. 27, No. 5, 1989, pp. 569–574. doi:10.2514/3.10147

[6] Liou, S., Komerath, N., and McMahon, H., "Velocity Measurements of Airframe Effects on a Rotor in Low-Speed Forward Flight," *AIAA Journal*, Vol. 26, No. 4, 1989, pp. 340–348.

[7] Liou, S., Komerath, N., and McMahon, H., "Velocity Field of a Cylinder in the Wake of a Rotor in Forward Flight," *AIAA Journal*, Vol. 27, No. 9, 1990, pp. 804–809. doi:10.2514/3.45940

[8] Kim, J., and Komerath, N., "Summary of the Interaction of a Rotor Wake with a Circular Cylinder," *AIAA Journal*, Vol. 33, No. 3, 1995, pp. 470–478. doi:10.2514/3.12600

[9] Freeman, C., and Mineck, R., "Fuselage Surface Pressure Measurements of a Helicopter Wind-Tunnel Model with a 3.15-Meter Diameter Single Rotor," NASA, TM-80051, 1979.

[10] Elliott, J., Althoff, S., and Sailey, R., "Inflow Measurements Made with a Laser Velocimeter on a Helicopter Model in Forward Flight—Volume 1: Rectangular Planform Blades at an Advance Ratio of 0.15," NASA TM-100541, 1988.

[11] Elliott, J., Althoff, S., and Sailey, R., "Inflow Measurements Made With a Laser Velocimeter on a Helicopter Model in Forward Flight—Volume 2: Rectangular Planform Blades at an Advance Ratio of 0.23," NASA TM-100541, 1988.

[12] Chaffin, M., and Berry, J., "Navier–Stokes and Potential Theory Solutions for a Helicopter Fuselage and Comparison with Experiment," NASA TM-4566, 1994.

[13] Mineck, R., and Althoff Gorton, S., "Steady and Periodic Pressure Measurements on a Generic Helicopter Fuselage Model in the Presence of a Rotor," NASA TM-2000-210286, 2000.

[14] Sides, J., Pahlke, K., and Costes, M., "Numerical Simulation of Flows Around Helicopters at DLR and ONERA," *Aerospace Science and Technology*, Vol. 5, No. 1, 2001, pp. 35–53. doi:10.1016/S1270-9638(00)01078-6

[15] Park, Y., Nam, H., and Kwon, O., "Simulation of Unsteady Rotor-Fuselage Aerodynamic Interaction Using Unstructured Adaptive Meshes," *American Helicopter Society 59th Annual Forum*, Phoenix, AZ, May 2003.

[16] Park, Y., and Kwon, O., "Simulation of Unsteady Rotor Flow Field Using Unstructured Adaptive Sliding Meshes," *Journal of the American Helicopter Society*, Vol. 49, No. 4, 2004, pp. 391–400.

[17] Nam, H., Park, Y., and Kwon, O., "Simulation of Unsteady Rotor-Fuselage Aerodynamic Interaction Using Unstructured Adaptive Meshes," *Journal of the American Helicopter Society*, Vol. 51, No. 2, 2006, pp. 141–148. doi:10.4050/JAHS.51.141

[18] Renaud, T., Benoit, C., Boniface, J.-C., and Gardarein, P., "Navier–Stokes Computations of a Complete Helicopter Configuration Accounting for Main and Tail Rotor Effects," 29th European Rotorcraft Forum, Friedrichshafen, Germany, Council of European Aerospace Societies Paper 42, Sept. 2003.

[19] Renaud, T., Le Pape, A., and Benoit, C., "Unsteady Euler and Navier–Stokes Computations of a Complete Helicopter Configuration," 31st European Rotorcraft Forum, Florence, Italy, Council of European Aerospace Societies Paper 99, Sept. 2005.

[20] Affes, H., Conlisk, A., Kim, J., and Komerath, N., "Model for Rotor Tip Vortex-Airframe Interaction, Part 2: Comparison with Experiment, Vortex Wake Interaction," *AIAA Journal*, Vol. 31, No. 12, 1993, pp. 2274–2282. doi:10.2514/3.11925

[21] Affes, H., Xiao, Z., Conlisk, A., Kim, J., and Komerath, N., "Model for Rotor Tip Vortex-Airframe Interaction, Part 3: Viscous Flow on Airframe, Vortex Wake Interaction," *AIAA Journal*, Vol. 36, No. 3, 1998, pp. 409–415. doi:10.2514/2.378

[22] Komerath, N., Mavris, D., and Liou, S., "Prediction of Unsteady Pressure and Velocity over a Rotorcraft in Forward Flight," *Journal of Aircraft*, Vol. 28, No. 8, 1991, pp. 509–516. doi:10.2514/3.46056

[23] Hariharan, N., and Sankar, L., "Unsteady Overset Simulation of Rotor-Airframe Interaction," *Journal of Aircraft*, Vol. 40, No. 4, 2003, pp. 662–674. doi:10.2514/2.3170

[24] Schwarz, T., "The Overlapping Grid Technique for the Time Accurate Simulation of Rotorcraft Flows," *31st European Rotorcraft Forum*, Florence, Italy, Sept. 2005.

[25] Khier, W., Schwarz, T., and Raddatz, J., "Time Accurate Simulation of the Flow around the Complete BO105 Wind Tunnel Model," *31st European Rotorcraft Forum*, Florence, Italy, Sept. 2005.

[26] Potsdam, M., Yeo, H., and Johnson, W., "Rotor Airloads Prediction Using Loose Aerodynamic/Structural Coupling," *American Helicopter Society 60th Annual Forum*, Baltimore, MD, June 2004.

[27] O'Brien, D., "Analysis of Computational Modeling Techniques for Complete Rotorcraft Configurations," Ph.D. Thesis, Georgia Inst. of Technology, Atlanta, 2006.

[28] Jameson, A., "Time Dependent Calculations Using Multigrid, with Applications to Unsteady Flows Past Airfoils and Wings," 10th Computational Fluid Dynamics Conference, Honolulu, HI, AIAA Paper 1991-1596, June 1991.

[29] Morvant, R., Badcock, K., Barakos, G., and Richards, B., "Aerofoil-Vortex Interaction Using the Compressible Vorticity Confinement Method," *AIAA Journal*, Vol. 43, No. 1, 2004, pp. 63–75. doi:10.2514/1.5177

[30] Spentzos, A., Barakos, G., Badcock, K., Richards, B., Wernert, P., Schreck, S., and Raffel, M., "CFD Investigation of 2D and 3D Dynamic Stall," *AIAA Journal*, Vol. 43, No. 5, 2005, pp. 1023–1033. doi:10.2514/1.8830

[31] Steijl, R., and Barakos, G., "A Computational Study of the Advancing Side Lift Phase Problem," *Journal of Aircraft*, Vol. 45, No. 1, 2008, pp. 246–257. doi:10.2514/1.22044

[32] Steijl, R., and Barakos, G., "Computational Analysis of Rotor-Fuselage Interactional Aerodynamics Using Sliding-Plane CFD Method," 34th European Rotorcraft Forum, Liverpool, England, U.K., Royal Aeronautical Society, Paper 3b2, Sept. 2008.

S. Fu
Associate Editor